ADVANCED ENERGY & SUSTAINABILITY RESEARCH
www.advenergysustres.com

Microwave-Assisted Synthesis of Cobalt-Based Selenides as Catalyst Precursors for the Alkaline Water Oxidation

Eleanora Charnetskaya, Tam D. Nguyen, Khang N. Dinh, Darcy Simondson, Sam Johnston, Carlos Felipe Garibello, Dijon A. Hoogeveen, Bernt Johannessen, Douglas R. MacFarlane, Rosalie K. Hocking, Manjunath Chatti, and Alexandr N. Simonov**

When used to promote the oxygen evolution reaction (OER), transition-metal chalcogenides convert into oxyhydroxide/(hydr)oxide catalysts, the performance of which depends on the properties of the precursor. The present study aims to explore these effects for cobalt and cobalt–iron selenides ($CoSe_n$ and $Co_1Fe_1Se_n$) prepared using a simple microwave-assisted method, in comparison to a reference material synthesized by high-temperature reaction of CoO_xH_y with Se vapors. Physical characterization of the microwave-synthesized $CoSe_n$ demonstrates their sheet-like morphology and identifies Co_3Se_4 as the major phase, which is essentially completely transformed into CoOOH during the OER. The temperature during the microwave-assisted $CoSe_n$ synthesis affects the crystallinity, the electrochemically active surface area, and thereby the performance of the resulting catalysts. Further improvements in the activity are achieved by combining cobalt with iron into a bimetallic $Co_1Fe_1Se_n$ precursor, which transforms in situ into a CoOOH + FeOOH composite and sustains the OER rate of 100 mA cm^{-2} (33 A g^{-1}) at an overpotential of $\approx$0.31 and 0.26 V at 24 $\pm$ 2 and 80 $\pm$ 1 °C, respectively. Satisfactory stability of the $Co_1Fe_1Se_n$-derived electrodes is demonstrated through a 4-day-long test at 80 $\pm$ 1 °C and 100 mA cm^{-2}.

1. Introduction

Effective electrodes for practical alkaline water electrolysis are required to support the global transition towards the use of sustainably produced hydrogen for the chemical industry and energy storage. Although the cathodic hydrogen evolution reaction presents its own challenges at high pH,[1–6] the anodic oxygen evolution reaction (OER) remains a major contributor to the energy efficiency losses.[7,8] This stimulates continuous research and development activities from both industry and academia on the development of cheaper and better-performing alkaline water electrolysis anodes.[9]

Apart from the traditional catalysts based on oxyhydroxides/(hydr)oxides of the first row transition metals, researchers are also actively exploring chalcogenides, pnictides, and related compounds as alternatives.[10–12] Although these materials are thermodynamically unstable under the OER conditions and convert into corresponding oxyhydroxide/(hydr)oxide species,[13–15] this approach has demonstrated promise in creating better performing catalysts. The origins of the improvements might stem from the enhanced electrochemically active surface area due to the peculiar morphology of the precursors,[13,14,16,17] as well as from the improved conductivity provided by the formation of core–shell structures based on a better-conducting intact precursor coated with

E. Charnetskaya, T. D. Nguyen, K. N. Dinh, D. Simondson, S. Johnston, D. A. Hoogeveen, D. R. MacFarlane, M. Chatti, A. N. Simonov
School of Chemistry
Monash University
Clayton, Victoria 3800, Australia
E-mail: manjunath.chatti1@monash.edu;
alexandr.simonov@monash.edu

The ORCID identification number(s) for the author(s) of this article can be found under https://doi.org/10.1002/aesr.202300108.

[Correction added on 12 February 2025, after first online publication: the affiliation of the eighth author has been corrected in this version.]

DOI: 10.1002/aesr.202300108

C. F. Garibello, R. K. Hocking
Department of Chemistry and Biotechnology
Swinburne University of Technology
Hawthorn, Victoria 3266, Australia

B. Johannessen
Australian Synchrotron
ANSTO
800 Blackburn Rd, Clayton VIC 3168, Australia

catalytically active but poorly conducting (oxy)hydroxide-based species.[18–20] Electronic effects have been also proposed to support improvements in the activity.[18,21–25]

A significant body of research on the transition-metal sulfides as OER catalyst precursors has been reported over the last decade, with a range of outstanding results achieved.[21,26–28] More recently, selenides have captured increased attention as an alternative class of chalcogenides. The energy level of the Se 3*d* orbital is close to those of the 3*s* and 3*p* orbitals of some transition metals like Co, Ni, Fe, and others.[29–31] As a result, the transition-metal selenides can exhibit metallic properties, which facilitate electron transfer and electrochemical transformations.[32] These properties can promote the formation of efficient OER catalysts from the selenide precursors at positive potentials.

Among selenides examined to date as precursors for the alkaline OER, some of the best results were obtained with the cobalt-based materials.[27,33–35] Some studies ascribe this to a favorable electronic configuration of $CoSe_2$ ($t_{2g}^6e_g^1$),[36] which is hypothesized to be close to optimal for a high-performance OER catalyst.[37] This interpretation is questionable since the selenide phase is highly unstable during the OER and is inevitably transformed, at least on the surface where the reaction occurs, into cobalt oxyhydroxide.[31] Arguably, more relevant are the metallic properties of cobalt selenide, as confirmed by both theoretical[31,36] and experimental[30] studies, which provide high electrical conductivity. Zhang et al. demonstrated transformation of $CoSe_2$ into CoOOH and suggested that the latter contains increased number of low-coordination Co atoms, which could increase the OER activity.[31] The same report also suggested that the growth of active CoOOH sites on the $CoSe_2$ surface might be facilitated by the anion vacancies.

One property of the cobalt selenide materials that can be further improved to produce better OER catalysts is the density of active sites on the surface. This can be addressed through the synthesis of high-surface-area $CoSe_n$ precursors, which is sometimes challenging to achieve with the conventional synthetic methods, especially those involving treatment at elevated temperatures. A method that has proven to produce highly dispersed nanomaterials of various compositions, including chalcogenides for the catalysis of water electrolysis,[28,38,39] is the microwave-assisted synthesis. This approach is well known to generate materials with enhanced electrochemically active surface area and to enable fine control over the morphology of the products.

Herein, we present a fast, microwave-assisted synthesis of cobalt and also cobalt–iron selenides using sodium selenite as a Se source, rather than significantly more hazardous selenium vapors. Upon electrooxidation, the resulting selenide materials are demonstrated to produce active and robust alkaline OER catalysts.

2. Results and Discussion

2.1. Structure and Morphology

Cobalt selenide synthesized through a two-stage process using selenium vapors on the surface of the F-doped SnO_2 (FTO) electrodes (see Experimental; Figures S1 and S2, Supporting Information) was used as a reference benchmark herein. X-ray diffraction (XRD) analysis of the electrodes at different stages of this synthesis confirmed the expected sequence of chemical transformations (Figure S3, Supporting Information). In the first step, a mixture of highly disordered Co_3O_4 and possibly $Co(OH)_2$ producing very weak reflections was formed.[40,41] Subsequent treatment with selenium vapors provided by heating at 350 °C over 2 h (preceded by ≈2 h preheating) in the presence of 20 mg of the Se powder produced a hard to decipher mix of compounds, but a 50% increase in the amount of selenium loaded in the tubular furnace enabled complete conversion of the oxide and hydroxide precursors into Co_3Se_4 (Figure S3, Supporting Information). Mean size of the resulting cobalt selenide crystallites calculated from the full width at half maximum of the (111) reflection was approximately d_{XRD} ≈12 nm. The amount of Co_3Se_4 produced on FTO in this manner was approximately 10 mg cm^{-2}, as determined by weighing the functionalized electrode before and after treatment with 15.7 M HNO_3, washing with water and drying.

The same Co_3Se_4 phase was also formed after just 1 h of a microwave-assisted reaction between dissolved cobalt(II) acetate and sodium selenate at much lower temperatures (**Figure 1**a). Even at 150 °C, a highly disordered material exhibiting a very broad (111) reflection of cobalt selenide was produced. A much better defined Co_3Se_4 phase was detected after the reaction at 180 ($d_{XRD} \approx 16$ nm) and 200 °C ($d_{XRD} \approx 15$ nm). However, an additional diffraction peak at ≈5° corresponding to an unidentified admixture was present in the material synthesized at 200 °C. Hence, the major focus of further characterization studies was on the material obtained at 180 °C.

The Raman spectrum of the microwave-synthesized $CoSe_n$ (Figure 1b) exhibits a set of signals consistent with previous reports on cobalt selenides synthesized via different methods.[42,43] Specifically, peaks at 184 and 681 cm^{-1} can be attributed to the A_g and A_{1g} vibration modes of $CoSe_n$, respectively.[42,44–48] A broader band at 138 cm^{-1} can be assigned to a E_g vibration mode of the Se atoms, while signals at 476, 520, and 611 cm^{-1} might correspond to the E_g, $1F_{2g}$, and $2F_{2g}$ modes of CoO_x from the partially oxidized surface of the material.[36,45–47,49]

Scanning (SEM) and transmission electron microscopy (TEM) imaging of the microwave-synthesized $CoSe_n$ suggests that the material represents aggregates ranging in size from dozens to a few hundred nanometers (**Figure 2**a,b). These aggregates comprise small crystallites with clearly defined lattice fringes with an interlayer distance of approximately 0.26–0.27 nm, which is consistent with the (111) plane of the Co_3Se_4 phase (PDF 04-015-1918). The uniformity of the distribution of Co and Se elements throughout the material was confirmed by energy-dispersive X-ray spectroscopic (EDS) mapping under the SEM conditions, which is consistent with the formation of a single major cobalt selenide phase (Figure 2c). The composition of the microwave-synthesized $CoSe_n$ estimated from the EDS/SEM data was relatively consistent, considering the quantification limitations of the technique, with a cobalt:selenium ratio of 1:1 derived from the inductively coupled plasma optical emission spectrometric (ICP–OES) analysis (Table S1, Supporting Information).

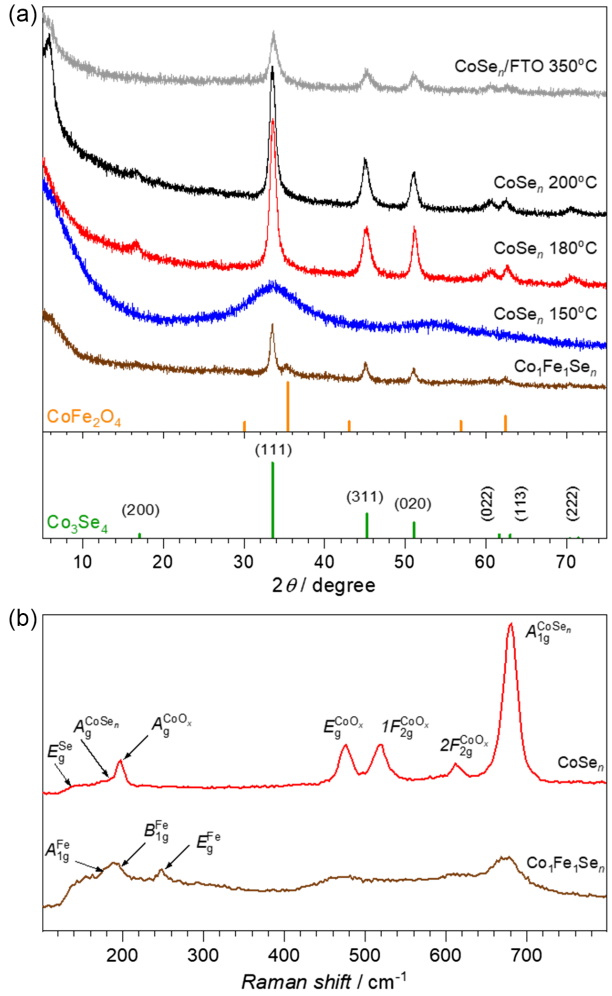

Figure 1. a) X-ray diffraction (XRD) patterns and b) Raman spectra of the investigated materials. Data are shown for the CoSe$_n$ produced by the microwave-assisted method at 150 (blue), 180 (red), and 200 °C (black), and for the microwave-synthesized Co$_1$Fe$_1$Se$_n$ (brown); data for the CoSe$_n$/FTO sample produced via a high-temperature selenidation are shown as grey trace. Vertical lines in panel a show tabulated positions and relative intensities for Co$_3$Se$_4$ (PDF 04-015-1918) and CoFe$_2$O$_4$ (PDF 00-022-1086). In panel b, labels show peak assignments based on the literature data.[36,42,45–49,65–68]

X-ray photoelectron spectroscopy (XPS) survey scans verify the presence of Co and Se, along with C and O, as expected (Figure S4 and S5, Supporting Information). The high-resolution Co 2*p* spectrum exhibits a set of signals typical of oxide/hydroxide of cobalt with an oxidation state close to 2+, as suggested by the intense satellite peaks,[50] along with well-defined components at lower binding energies of ≈778 and 793 eV, which can be confidently assigned to the cobalt selenide species[51] (Figure S5a, Supporting Information). The high-resolution Se 3 d scan has a prominent set of signals at ≈55 eV, which can be attributed to a Se–Co bond, as well as signals at higher binding energies corresponding to the oxidized states of selenium (Figure S5b, Supporting Information). Thus, XPS analysis indicates that the surface of the microwave-synthesized cobalt selenide is partially oxidized, as is commonly found for chalcogenides of transition metals. Nevertheless, the surface ratio of the cobalt and selenium concentrations derived from XPS was still close to 1:1, consistent with the bulk composition.

Co K-edge X-ray absorption near edge structure (XANES) data for the as-synthesized CoSe$_n$ are akin to that reported for cobalt sulfides in the literature and suggest an oxidation state of the metal ≤2+ (**Figure 3**a). The Co K-edge extended X-ray absorption fine structure (EXAFS) and its Fourier transform (FT) was not consistent with the Co(OH)$_2$ structure (Figure S6, Supporting Information), attesting to the formation of a selenide phase, in agreement with the XRD data (Figure 3a).

The use of the CoSe$_n$ to catalyze the OER in 1 M KOH for 24 h at 10 mA cm^{-2} and 23 ± 2 °C (vide infra) resulted in oxidation of cobalt and produced Co K-edge X-ray absorption spectroscopy (XAS) data that almost perfectly match that for the CoOOH reference (Figure 3a and S6, Supporting Information). In situ Co K-edge XANES data recorded at increasingly positive potentials confirm progressive oxidation of cobalt and demonstrate that the process is irreversible, as concluded from the comparisons of the data recorded at 1.15 V versus reversible hydrogen electrode (RHE) before and after polarizations at up to 1.95 V versus RHE (Figure 3b). At the same time, these data indicate that the transformation is not instantaneous and several hours of continuous operation are required for complete bulk conversion of the examined selenide material into CoOOH.

In anticipation of the promoting effect of incorporating iron on the OER activity of the selenide-derived electrocatalysts, we also explored the synthesis of Co$_1$Fe$_1$Se$_n$. In this case, cobalt–iron (1:1 mol) layered double hydroxides (Co$_1$Fe$_1$-LDH) were used as a precursor for the microwave-assisted reaction with Na_2SeO_3 with the aim of achieving maximal homogeneity of intermixing the two metals in the selenide structure, as well as to demonstrate the possibility of using solid precursors for the low-temperature solution-based selenidation. The temperature maintained during the synthesis was 180 °C, which was found to be optimal for the formation of the monometallic cobalt selenide, as discussed earlier. The XRD pattern of the microwave-synthesized Co$_1$Fe$_1$Se$_n$ powder was similar to that of CoSe$_n$, i.e., consistent with a Co$_3$Se$_4$-type phase (Figure 1a). The mean crystallite size in this case was ≈13 nm. There was also an additional diffraction signal appearing at ≈35.3°, which might be associated with a CoFe$_2$O$_4$ admixture. The Raman spectrum of Co$_1$Fe$_1$Se$_n$ was also qualitatively similar to that of CoSe$_n$, but with all characteristic peaks associated with cobalt broadened and significantly suppressed in intensity (Figure 1b). It is also likely that these signals were overlapped with a B_{1g} peak at 196 cm^{-1} of Fe vibrations, which also include a E_g peak at 248 cm^{-1}.[52] The slightly different position of the A_{1g}^{Se} peak for Co$_1$Fe$_1$Se$_n$ as compared to that recorded for CoSe$_n$ might be possibly associated with the change in the selenium–metal bond lengths.

SEM analysis of Co$_1$Fe$_1$Se$_n$ reveals more homogeneous distribution and relatively lower size of the aggregates as compared to CoSe$_n$ (**Figure 4**a), while the TEM again reveals highly dispersed nanocrystallites (Figure 4b). All three key elements are homogeneously distributed within the material, as suggested by the EDS/SEM mapping (Figure S7a, Supporting Information) with a Co:Fe:Se ratio of ≈1:1:3. The ICP–OES analysis confirmed that the two metals are present in a close to equimolar ratio (Table S1,

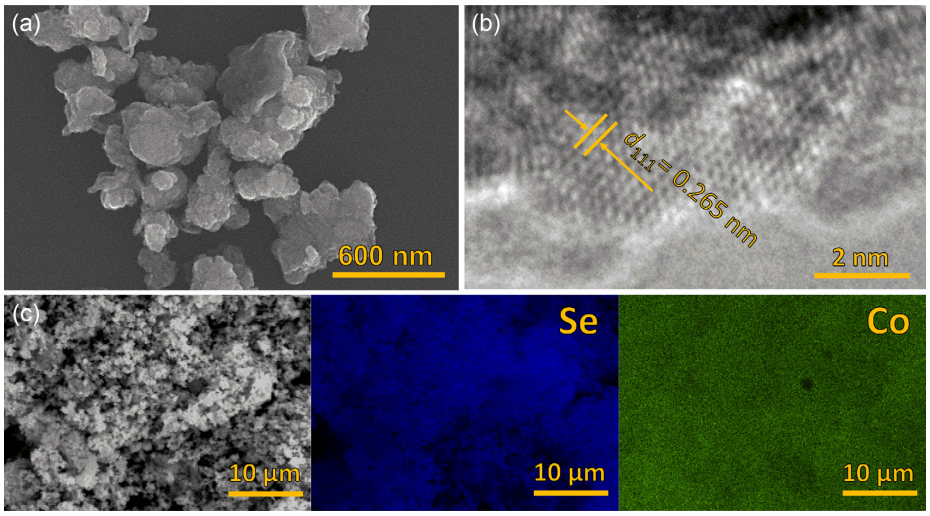

Figure 2. a) Scanning and b) transmission electron micrographs, and c) EDS/SEM mapping of $CoSe_n$ synthesized using the microwave-assisted method at 180 °C.

Supporting Information). After the use of $Co_1Fe_1Se_n$ to promote the OER for 96 h in 1 M KOH at 80 ± 1 °C and a constant current density of 100 mA cm^{-2} (vide infra), a significant change in the morphology occurred (Figure 4c). After such harsh treatment, the material transformed into globular aggregates of high surface area nanosheets, which is consistent with the expected formation of the (oxy)hydroxides of cobalt and iron. A substantial, though incomplete, loss of selenium was confirmed by the EDS/SEM results (Figure S7b and Table S1, Supporting Information).

XPS analysis of the $Co_1Fe_1Se_n$ confirms the presence of all key elements (Figure S8, Supporting Information) and also indicates that the surface of the as-prepared material is dominated by selenides (707 and 720 eV in Fe $2p$[51]; 778 and 793 eV in Co $2p$[51]) but not (hydr)oxides of cobalt and iron (Figure S9, Supporting Information). Moreover, selenide rather than [Se–O] species produces predominant signals in the Se 3 d spectrum (Figure S9c, Supporting Information). Nevertheless, operation of the material as an OER catalyst (96 h at 100 mA cm^{-2} and 80 ± 1 °C in 1 M KOH) again results in complete removal of the surface selenide species and most likely produces Co^{3+} and Fe^{3+} (oxy)hydroxides (Figure S9a,b, Supporting Information).

The Co K-edge XANES and EXAFS of the as-prepared $Co_1Fe_1Se_n$ were essentially identical to those of the $CoSe_n$ material, consistent with the XRD, Raman, and XPS data (Figure 3a and S6, Supporting Information). Furthermore, Fe K-edge XAS data for the microwave-synthesized bimetallic material strongly resembled that for a mackinawite FeS_m reference, indicating a very similar iron chemical state in the sulfides and selenides (Figure 3c and S6, Supporting Information). Interestingly, the use of $Co_1Fe_1Se_n$ to sustain a 48-h-long OER experiment under harsh conditions of 100 mA cm^{-2} and 80 ± 1 °C did not result in complete oxidation of cobalt into CoOOH, with a lower oxidation state component still present (Figure 3a and S6, Supporting Information). At the same time, iron selenide was quantitatively transformed into iron oxyhydroxide, as evidenced by both XANES (Figure 3a) and EXAFS (Figure S6, Supporting Information).

Overall, all physical characterization methods employed clearly attest to the formation of selenides of cobalt and iron under the microwave-synthesis conditions employed herein, either with the use of dissolved or solid metal precursors. The use of these materials to promote the OER results in their transformation into corresponding oxyhydroxides, which catalytic activity is discussed below.

2.2. Electrocatalytic Activity

All electrochemical studies herein used 1 M KOH electrolyte and were undertaken either at ambient (23 ± 2 °C) or elevated temperatures (40 ± 1 and 80 ± 1 °C). Testing the microwave-synthesized $CoSe_n$ deposited either on a flat (glassy carbon [GC]) or porous (carbon fiber paper [CFP]) substrates at a medium loading (≈0.28 mg cm^{-2}) as a H_2 evolution catalyst did not produce any noteworthy results. Specifically, the current density of −10 mA cm^{-2} (hereinafter, per geometric surface area of the electrode), which corresponds to approximately −36 A g^{-1}, required an overpotential of 0.4–0.45 V at 23 ± 2 °C (Figure S10, Supporting Information). Thus, further tests focused exclusively on the OER.

First, we confirmed that the temperature of 180 °C during the microwave-assisted synthesis produces a $CoSe_n$ precursor of the more active catalysts than provided by 150 and 200 °C. Indeed, cyclic voltammograms recorded before and after extended galvanostatic tests at 10 mA cm^{-2}, and the chronopotentiometric data itself, indicated that the material produced at 180 °C enables better activity (Figure S11, Supporting Information). Specifically, the potential required to sustain the OER rate of 10 mA cm^{-2} (23 ± 2 °C) was ≈1.51, 1.48, and 1.50 V versus RHE for the synthesis temperatures of 150, 180, and 200 °C, respectively (Figure S11b, Supporting Information). Although the differences in the activity were not very significant, they were still beyond the error of reproducibility of the synthetic procedure, which was satisfactorily high (Figure S12, Supporting Information). Better performance provided by the $CoSe_n$ precursor prepared at 180 °C is likely associated with the higher concentration of

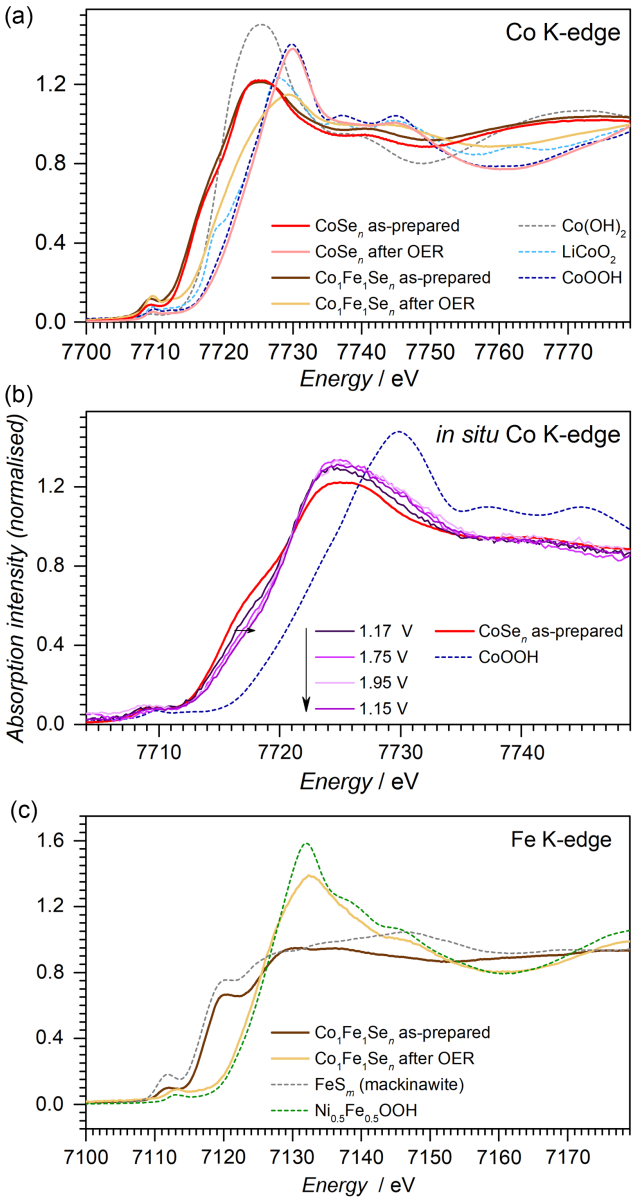

Figure 3. X-ray absorption near edge structure of the microwave-synthesized materials. a) Ex situ Co K-edge data for $CoSe_n$ before (red) and after the OER test (pink), and $Co_1Fe_1Se_n$ before (brown) and after the OER test (yellow). b) In situ Co K-edge data for $CoSe_n$ collected at potentials changed in the following sequence (shown by arrows): 1.15, 1.75, 1.95, and 1.15 V versus RHE, compared to the data for the as-prepared material (red). c) Fe K-edge data for $Co_1Fe_1Se_n$ before (brown) and after the OER test (yellow). Dashed lines show reference data for $Co(OH)_2$ (grey), $LiCoO_2$ (light blue), CoOOH (dark blue), FeS_m (grey), and $Ni_{0.5}Fe_{0.5}OOH$ (green). OER tests for ex situ experiments were undertaken in 1 M KOH at 10 mA cm^{-2} and 23 ± 2 °C for 24 h ($CoSe_n$), and at 100 mA cm^{-2} and 80 ± 1 °C for 48 h ($Co_1Fe_1Se_n$). In situ measurements were undertaken in 1 M KOH at 23 ± 2 °C.

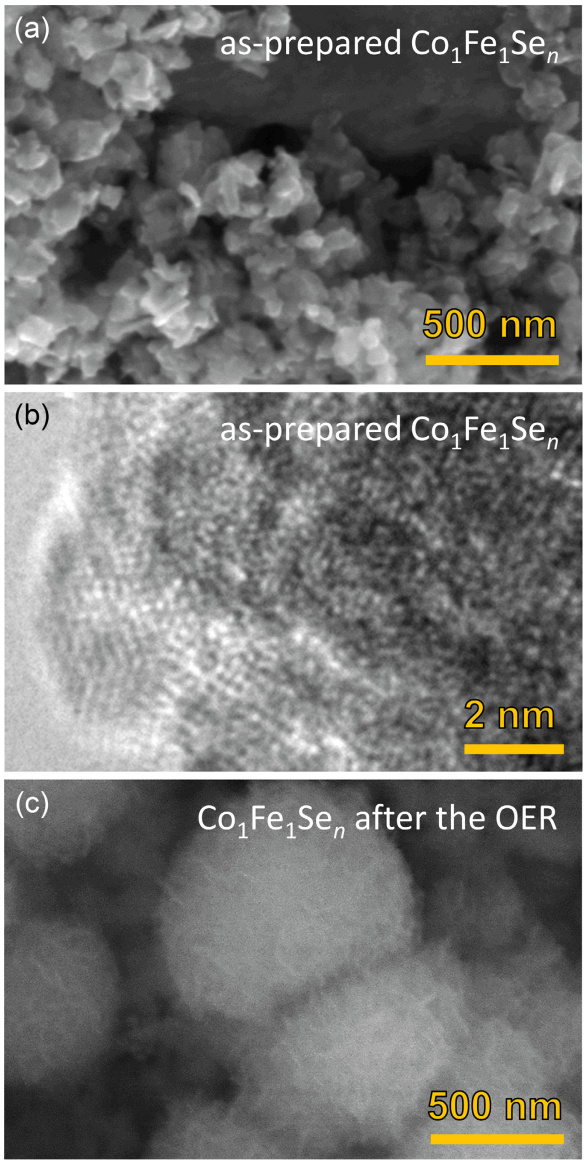

Figure 4. Microscopic characterization of the microwave-synthesized (180 °C) $Co_1Fe_1Se_n$ a,b) before and c) after OER test at 100 mA cm^{-2} and 80 ± 1 °C for 96 h in 1 M KOH: a,c) SEM and b) TEM images.

redox active Co sites on the surface of the catalyst derived from this material, as suggested by cyclic voltammetric data (inset to Figure S11a, Supporting Information). The presence of admixtures in the material synthesized at 200 °C and excessive disorder of $CoSe_n$ prepared at 150 °C (Figure 1a) might also contribute to the slightly lower catalytic performance. An important feature of the $CoSe_n$ materials during extended chronopotentiometric tests was continuous improvement in the OER activity (Figure S11b, Supporting Information). This observation is consistent with the physical characterization data provided earlier, in particular in situ and ex situ XAS (Figure 3 and S6, Supporting Information), which indicate progressive transformation of the selenide to the catalytically active CoOOH. However, we also note that these initial tests were aimed at semiquantitative screening of the activity and were undertaken using inherently unstable carbon fiber electrodes, which might have also contributed to the oxidation currents. To avoid any ambiguities, all further experiments used stable FTO and Ni mesh substrates.

It was important to compare the OER catalytic performance provided by the microwave-synthesized $CoSe_n$ to that of the material obtained by high-temperature selenidation. As discussed earlier, both methods produced the same Co_3Se_4 phase according to XRD, although the loading of the material on the electrode was very different. Specifically, the microwave-synthesized $CoSe_n$ was loaded at 0.28 mg cm^{-2} onto an FTO electrode, while the one produced by the high-temperature two-step method contained ≈10 mg cm^{-2} of the material. When used for the OER, these electrodes produced comparable activity, though the one modified with a much lower amount of $CoSe_n$ produced in a one-step microwave-assisted reaction was even slightly better in performance (Figure S13, Supporting Information). Higher density of the redox active cobalt species provided by the microwave method additionally highlights the advantages of this synthetic approach, in addition to the lack of a need to use hazardous Se vapors and higher temperatures.

Further tests focused on the $Co_1Fe_1Se_n$ material, with the aim to understand if the intentional introduction of a significant amount of iron species into the precursor would produce a better performing catalyst[53,54] than that derived from $CoSe_n$ (note that no measures were taken to remove the Fe admixtures from the electrolyte). For both types of materials, the key catalytic species are most likely bimetallic Co–Fe sites; for $CoSe_n$, iron species might be introduced as a minor contaminant from the electrolyte, which was not subject to extensive purification in our study. When immobilized on a Ni mesh substrate, $Co_1Fe_1Se_n$ produced better performance than with the flat FTO substrate at the same level of loading, most likely due to the lower degree of agglomeration of the material (Figure S14, Supporting Information). We cannot completely exclude the potential promoting role of NiO_xH_y species that might be leached into the electrolyte solution from the electrode substrate and redeposited onto the $CoFeO_xH_y$ catalytic surface. Trace amounts of the oxidized forms of nickel were indeed detected by XPS after the OER, but it is important to recognize that Ni 2*p* signals were also found for the initial sample, and are most likely associated with the parts of the Ni mesh that were not completely coated with the catalyst (Figure S9, Supporting Information). We also note that the promoting effect of using the higher surface area Ni mesh support is seen for $Co_1Fe_1Se_n$ in the first voltammetric scans, which suggests that the potential role of NiO_xH_y leaching/redeposition is not significant. Thus, the nickel mesh substrate was used for the subsequent experiments.

During the initial cyclic voltammetric and short-term chronoamperometric tests, the bimetallic $Co_1Fe_1Se_n$ precursor provided better performance than $CoSe_n$ with an apparently lower slope of the overpotential (η) versus log j dependencies (**Figure 5**a,b and S15, Supporting Information). The latter difference is highly unlikely to be due to the alterations in the OER mechanisms with the two materials, since both develop the same catalytically active oxyhydroxide species on the surface. A more likely explanation is the timescales of the transformation of the selenide species into Co(Fe)OOH and potentially charge-transfer limitations within the catalyst layer produced in situ from $CoSe_n$ at elevated current densities. Moreover, the difference in the activity between the catalysts derived from $CoSe_n$ and $Co_1Fe_1Se_n$ progressively decreases during 15 h chronopotentiometric tests at a low current density of 10 mA cm^{-2}, indicating

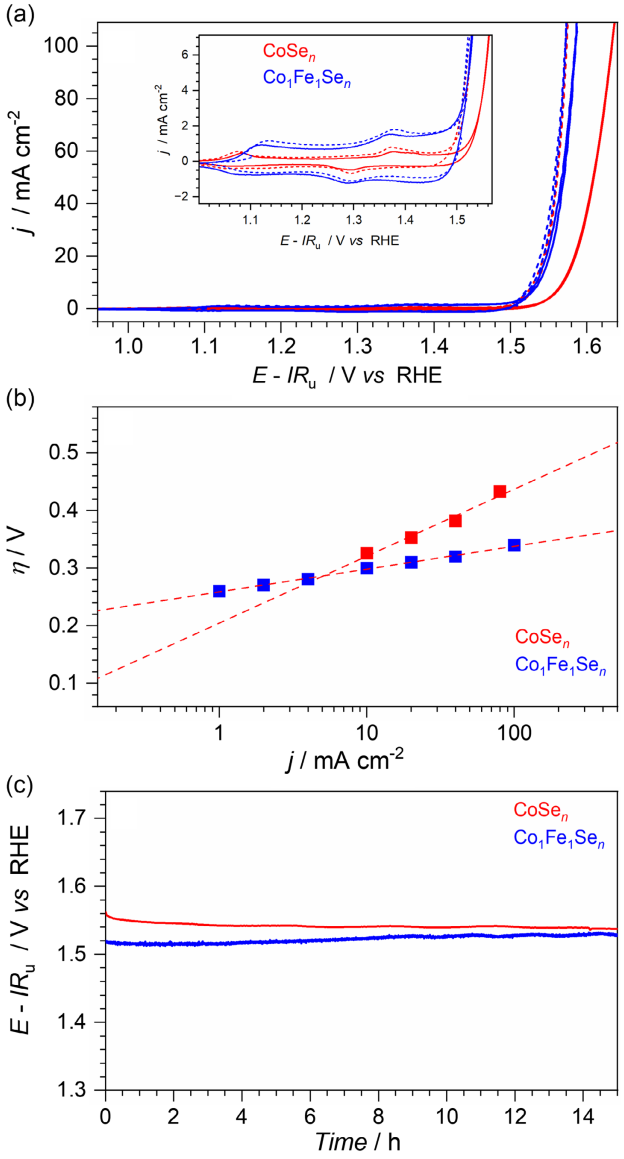

Figure 5. OER electrocatalytic activity of $CoSe_n$ (red) and $Co_1Fe_1Se_n$ (blue) synthesized by the microwave-assisted method at 180 °C and immobilized on Ni mesh electrodes using a PVDF-NMP binder at a loading of 0.28 mg cm^{-2} in 1 M KOH at 23 ± 2 °C: a) quasi-stabilized cyclic voltammetry (ν = 0.005 V s^{-1}; 5th scans) before (solid) and after (dashed) chronopotentiometric measurements shown in panel c (peaks at 1.3–1.4 V are associated with the Ni mesh substrate, which is not completely blocked with the thin catalyst layer at a relatively low loading used for these experiments); b) Tafel plots derived from the short-term chronopotentiometric measurements shown in Figure S15a,b, Supporting Information; and c) galvanostatic tests at 10 mA cm^{-2}. All data were manually post-corrected for the IR_u-drop. Currents are normalized to the geometric surface area of the electrodes (0.25 cm^2).

that similar catalytic species are eventually produced (Figure 5c), as also confirmed by cyclic voltammetry (Figure 5a).

Further studies focused on $Co_1Fe_1Se_n$, which presented better charge-transfer characteristics at higher current densities as compared to $CoSe_n$ (Figure 5b). The bimetallic selenide was deposited onto nickel mesh substrates at a higher loading of

3 mg cm^{-2} in an attempt to demonstrate electrodes with increased areal performance, as is commonly done in the field. The electrochemical impedance spectra collected at 1.53 V vs. RHE for such electrodes before and after a 24-h-long OER test at 100 mA cm^{-2} and ambient temperature demonstrated a slight decrease in the charge-transfer resistance of the catalytic reaction, which is consistent with the transformation of the selenide into more catalytically active oxyhydroxide species (Figure S16, Supporting Information). No modeling of the impedance data was undertaken due to the high level of uncertainty and limited value of the derived parameters.

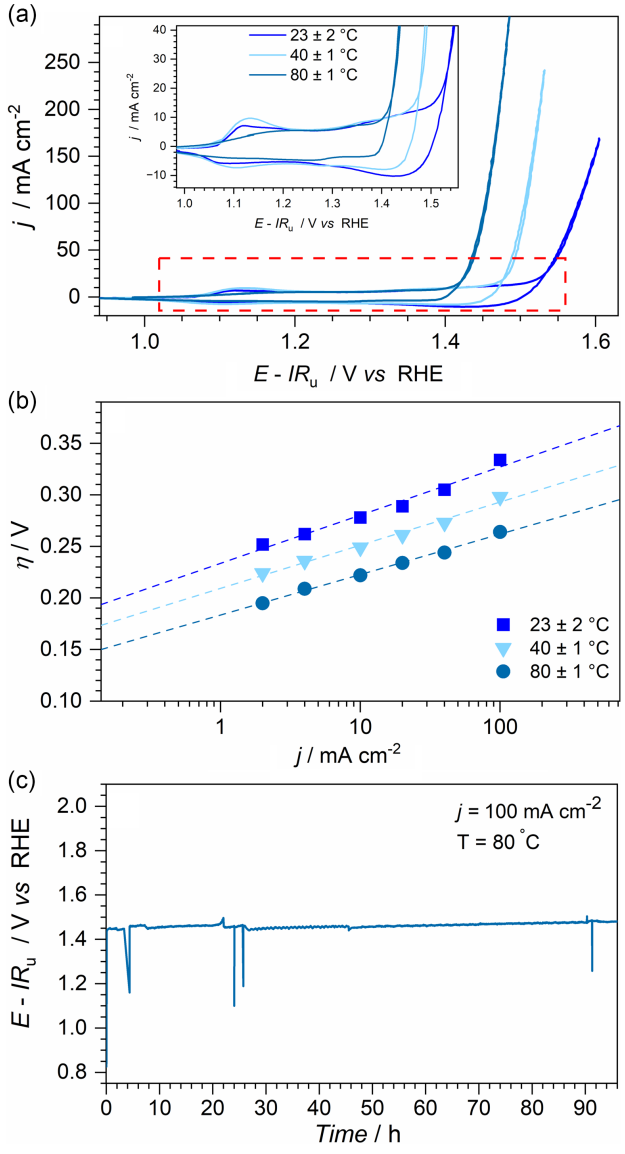

Figure 6. OER electrocatalytic activity of $Co_1Fe_1Se_n$ synthesized by the microwave-assisted method at 180 °C and immobilized on the Ni mesh electrodes using PVDF-NMP binder at a loading of 3 mg cm^{-2} in 1 M KOH at 23 ± 2, 40 ± 1, and 80 ± 1 °C: a) quasi-stabilized cyclic voltammetry ($\nu = 0.005$ V s^{-1}; 5th scans); b) Tafel plots derived from the short-term chronopotentiometric measurements shown in Figure S15c, Supporting Information; c) galvanostatic test at 80 ± 1 °C at a current density of 100 mA cm^{-2}. All data were manually post-corrected for the IR_u-drop. Currents are normalized to the geometric surface area of the electrodes (0.25 cm^2).

We demonstrated that the activity of the microwave-synthesized $Co_1Fe_1Se_n$ can be improved approximately 2.5-fold through the recently reported simple saline–alkaline activation procedure[55] without losses in the stability (Figure S17, Supporting Information). The activated $Co_1Fe_1Se_n$/Ni electrode enabled the OER rate of 100 mA cm^{-2} at 23 ± 2 °C at an overpotential of ≈0.31 V.

Further, the effect of temperature on the OER catalyzed by the $Co_1Fe_1Se_n$/Ni-mesh electrodes was examined. Cyclic voltammetry and short-term chronopotentiograms demonstrated expected performance improvements when increasing the electrolyte solution temperature from ambient to 40 ± 1 and 80 ± 1 °C (**Figure 6**a and S15c, Supporting Information). At all temperatures examined, the η versus log j data demonstrated a close to linear dependence up to 100 mA cm^{-2} with a slope within 0.04–0.05 V dec^{-1} (Figure 6b). This suggests the lack of significant charge/mass-transfer limitations as well as of substantial changes to the catalytic species during short-term chronopotentiometric tests.

Finally, robustness of the catalytic species formed on the $Co_1Fe_1Se_n$/Ni electrode was tested at 80 ± 1 °C and 100 mA cm^{-2} over 4 days. Under these conditions, the OER overpotential slowly increased over the initial ≈85 h to approximately 0.28 V and then remained stable (Figure 6c). To test if the loss in the activity was associated with the corrosion of the catalyst, ICP mass–spectrometric (MS) analysis of the electrolyte solution after the 4-day-long galvanostatic experiment was undertaken. Co and Fe were detected at the concentrations of 0.08 and 0.14 μM, respectively, which corresponds to the loss of less than 0.1 at% of the metals initially deposited onto the electrode (the value should be considered semiquantitative considering the uncertainties in the composition of the deposited $Co_1Fe_1Se_n$). The concentration of Se measured by ICP–MS in the solution was significantly higher (4.7 μM), though this amount still corresponds to only a few at% with respect to the amount deposited onto the electrode. Possibly, a significant portion of the oxidised selenium species might be retained within the bulk oxyhydroxide material. Overall, the level of stability of the OER catalysts derived from $Co_1Fe_1Se_n$ is satisfactory even at elevated temperatures.

3. Conclusions

The present study presents a simple and fast method for the synthesis of cobalt-based selenides that avoids the use of selenium vapors and instead employs dissolved sodium selenite as a source of Se. The method can be applied to both dissolved transition-metal precursors, as well as solid dispersions of hydroxides, as demonstrated by the examples of the synthesis of $CoSe_n$ and $Co_1Fe_1Se_n$. When subjected to the conditions of the alkaline OER, these materials transform into corresponding oxyhydroxides, although the conversion is not complete for the bimetallic material even after operation under harsh conditions of elevated temperature and current density. Oxidized selenium species might be retained within the bulk of $Co_1Fe_1Se_n$, suggesting that they might affect the catalytic performance. The OER activity

demonstrated herein is not record-breaking, but on par and sometimes better than that reported for the selenide-derived materials in the literature (see Table S2, Supporting Information, and ref. [56]). More importantly, the $Co_1Fe_1Se_n$-deirved catalyst demonstrates satisfactory robustness in operation at industrially relevant temperature of 80 ± 1 °C and suffers minimal, if any, loss of the catalytically active metals into the electrolyte solution. Given the ease of synthesis and high-surface-area morphology, the selenide materials presented herein might find use in other electrochemical applications.

4. Experimental Section

Materials: The following chemicals and reagents were used as received: cobalt(II) chloride hexahydrate (98%; Sigma–Aldrich), cobalt(II) acetate tetrahydrate (98%; Sigma–Aldrich), selenium powder (100 mesh, 99.5% trace metals basis; Sigma–Aldrich), iron(III) nitrate nonahydrate (≥98%; Sigma–Aldrich), N,N-dimethylformamide sodium selenite (99%; Sigma–Aldrich), diethylenetriamine (DETA, 99%; Sigma-Aldrich), hydrazine hydrate solution (24%–26% in H_2O [RT]; Sigma–Aldrich), carbamide (urea, 99.0%–100.5%; Sigma–Aldrich), poly(vinylidene fluoride) (PVDF; average $M_w \approx 534\,000$ by GPC, powder; Sigma–Aldrich), N–methyl-2-pyrolidone (NMP; 99.5%, anhydrous; Sigma–Aldrich), 2–propanol (ACS, ≥99.5%; Merck), ethanol absolute (≥99.5 vol%, analytical reagent; Ajax FineChem), and nitric acid (70%, Ajax FineChem).

Pt wire (0.5 mm diameter; 99.99%) was purchased from A&E Metals. Nickel mesh (0.2 mm thick, 99.994%) was obtained from Thermo Fisher Scientific. Glass coated with FTO was purchased from Dyesol Ltd. (TEC8 glass plates with a sheet resistance of 8 Ω sq^{-1}). CFP (060) was purchased from Toray. Zirfon UTP 500 + separator membrane for alkaline electrolysis (500 ± 50 µm, porosity 60 ± 5%) was purchased from Agfa-Gevaert NV. Adhesive Kapton polyimide tape was purchased from ProSciTech Pty Ltd.

High-purity H_2 and Ar (99.999%) were sourced from BOC. All solutions were prepared using deionized water with a resistivity of 18.2 MΩ cm at 23 ± 2 °C derived from Sartorius Arium Comfort I Ultrapure Water System H_2O-I-1-UV-T; the same quality water was used for all procedures whenever water was mentioned.

High-Temperature Synthesis of Cobalt Selenide: Aqueous solution (500 mL) of 0.15 M $CoCl_2$ and 1 M urea was prepared by first dissolving urea in a half-filled volumetric flask, then adding $CoCl_2$, and filling the flask with water to the mark. FTO supports were cut into 1 cm × 2 cm pieces, wrapped with Kapton tape leaving only a 1 cm × 1 cm square uncoated, and placed into the 25 mL Schott bottles aligned face down at an angle of 45°. The solution of cobalt chloride and urea was then poured into each bottle to completely cover the FTO. The bottles were placed into a silicon oil bath, preheated to 90 °C, and held at this temperature for 16 h (Figure S1a,b, Supporting Information). After the synthesis, FTO modified with cobalt hydroxide was kept inside the bottles to cool down naturally, thoroughly washed with water, and dried under the vacuum at 70 °C. The dried electrodes (Figure S1c, Supporting Information) were stored in a vacuum desiccator before being used in further synthesis of cobalt selenides.

Conversion of the FTO-supported CoO_xH_y into selenides was done in a tubular quartz furnace (internal diameter 66 mm; length 800 mm) at 350 °C (heating rate 3 °C min^{-1}) under ≈6 mL min^{-1} Ar flow for 2 h. Kapton tape was removed from the CoO_xH_y/FTO precursors, and they were placed in the middle of the furnace in an alumina boat, while the Se powder (20 or 30 mg) was added to another alumina boat that was positioned ≈4 cm away from the FTO-supported sample. The gas was flowing from Se toward CoO_xH_y/FTO. After the conversion, the samples were kept inside the furnace under the Ar flow until cooled down to ambient temperature.

Microwave-Assisted Synthesis of Cobalt Selenide: $CoSe_n$ and $Co_1Fe_1Se_n$ powders were synthesized in the microwave reactor (Discovery SP, CEM Corporation) using 35 mL vials in a dynamic mode where the microwave power was automatically adjusted to maintain preset temperature. For the synthesis, 15 mL of a mixed DETA:H_2O (2:1 vol) solvent was used. Water was slowly added into vigorously stirred DETA to avoid rapid heating and spillage of the mixture; the mixed solvent was kept in a closed flask under ambient conditions to cool down naturally. The DETA molecule with two primary amine groups could act as a mild reducing agent during the microwave synthesis, which reduced the reaction time and further alleviated the necessity of any additional reducing agents like hydrazine. The presence of water in the synthesis mixture promoted the formation of pure chalcogenide phases with high-surface-area morphology.[57]

To synthesize $CoSe_n$, 1 mmol of $Co(C_2H_3O_2)_2$ was added into the solvent mixture under continuous stirring and was sonicated (JPS-08 A, 40 Hz, 60 W; Vevor) for 5 min to facilitate dissolution (exemplified for $CoSe_n$ in Figure S2a, Supporting Information). Then, 1 mmol of Na_2SeO_3 was added under stirring, which caused the solution to lose its transparency (exemplified for $CoSe_n$ in Figure S2b, Supporting Information). Mixture was sonicated for another 30 min before being placed into the microwave reactor.

For the $Co_1Fe_1Se_n$ synthesis, the same solvent and the same preparation procedure were used, but 50 mg of cobalt–iron–LDH (Co_1Fe_1–LDH, synthesized by microwave accosted method described by Chatti et al.[28]) was used as a metal precursor and 30 mg of sodium selenite as a source of selenium. Co_1Fe_1–LDH was added into the solvent mixture under continuous stirring and was sonicated for 15 min; then Na_2SeO_3 was added under stirring and mixture was sonicated for 20 min prior to the microwave reaction.

The synthesis of $CoSe_n$ was carried out at three temperatures (150, 180, and 200 °C) for 1 h with a stirring option set to the "high"; $Co_1Fe_1Se_n$ was synthesized at 180 °C, which was as regarded as optimal. After the vial was removed from the reactor, the initially clear solution was transformed into a black suspension (Figure S2c, Supporting Information). The suspension was separated into the brown clear liquid and black powder after resting for 2 h under ambient conditions. Liquid was partially extracted by the syringe and the rest was transferred into three 5 mL centrifuge tubes and spun at 12 000 rpm for 6 min to separate the obtained material. The powder was washed with ethanol and water, and finally dried under vacuum at 70 °C. Typical yield of $CoSe_n$ was ≈50% and 72% when calculated with respect to cobalt acetate and selenite precursors, respectively. Typical yield of $Co_1Fe_1Se_n$ was ≈42% and 70% with respect to Co_1Fe_1–LDH and selenite precursors, respectively.

Electrochemical Measurements: Electrochemical measurements were undertaken in a three-electrode jacketed cell using a Bio-Logic VSP electrochemical workstation at ambient (23 ± 2 °C) or elevated temperature (40 ± 1 and 80 ± 1 °C) provided by a Polystat 1268-16 (Cole-Parmer Instrument Company) thermostat. Aqueous 1 M KOH (20 mL in the working electrode compartment) was used as an electrolyte solution for all experiments except of the experiments, in which the addition of Cl^- into electrolyte was studied, where 1 M KOH + 0.6 M NaCl (20 mL) was used. For the HER measurements, the solution was saturated with pure H_2 by purging the gas through for 30 min; further, the gas was slowly flown above the solution throughout the experiment. Stirring of the electrolyte solution with a Teflon-lined magnetic stirrer (10 mm length; 3 mm diameter; 500 rpm) was always applied to minimize the mass-transport effects, in particular those associated with the formation of gas bubbles on the electrode surface.

For the electrocatalytic tests, a GC electrode (3 mm diameter, 0.071 cm^2 geometric surface area; ItalSens Sensors), FTO (1 cm × 1 cm geometric surface area), CFP (0.5 × 0.5 cm geometric surface area) or Ni mesh (0.5 × 0.5 cm geometric surface area) were used as substrates. The surface of a GC electrode was polished on the felt disks with alumina powder (Alfa Aesar, particle size 1, 0.3, and 0.05 µm) two times for 30 s for each powder size with intense washing with water after each polishing step. Nickel mesh electrodes (geometric surface area 0.25 cm^2) were cut from a nickel mesh sheet and cleaned by sonication in water, immersion in HCl:H_2O (2:1 vol) for 2 min to remove surface oxides, and subsequent copious washing with water and sonicating in acetone, water, and absolute ethanol for 15 min in each solvent.

Catalysts (5 mg) were dispersed in 1 mL of a mixture of 0.70 mL of water, 0.25 mL of 2-propanol, and 0.05 mL of 8 wt% PVDF in NMP (PVDF-NMP) as a binder. The obtained suspensions were sonicated for 30 min (40 Hz, 50 W; Meinhardt Ultrasonics, Germany) and immediately drop-cast onto the surface of freshly cleaned GC, CFP, or FTO (loading 0.28 mg cm^{-2}) or Ni mesh electrodes (loading 0.28 or 3 mg cm^{-2}), and dried under N_2 flow for approximately 40–70 min.

The $CoSe_n$/FTO samples synthesized by a high-temperature selenidation method were used as working electrodes directly with Kapton tape reapplied to cover the unmodified parts of the surface.

The high surface area Pt wire auxiliary electrode was separated from the working electrode compartment with a low-porosity (P4) ceramic frit in all experiments conducted at room temperature and short-term experiments at elevated temperatures. In the long-term stability, experiments at 80 ± 1 °C, cathodic and anodic compartments were separated by a Zirfon membrane. A Hg|HgO|KOH(1 M) reference electrode was connected to the working electrode compartment through a salt bridge; the latter was fabricated by soaking a cotton thread in 1 M KOH and encapsulated inside a PTFE tube.[58] The tip of the salt bridge was aligned within a fixed distance of few millimeters from the working electrode surface. This reference system was calibrated against a custom-made RHE[59] in 1 M KOH at the required temperature. The potential of the reference electrode against RHE was 0.926 ± 0.000 V at 23 ± 2 °C, 0.916 ± 0.001 V at 40 ± 1 °C, and 0.893 ± 0.000 V at 80 ± 1 °C; all potentials in this work are reported on the RHE scale.

Uncompensated resistance (R_u) was derived from the electrochemical impedance spectra (frequency range from 200 kHz to 0.1 Hz; amplitude 0.010 V) recorded at potentials where no significant faradaic processes occurred (typically, 0.02–0.07 V vs. RHE). Measured R_u values for the CFP and Ni mesh working electrodes were within the range of 1–3 Ω depending on the temperature; for the FTO electrodes, the R_u was between 20 and 25 Ω. The reported potentials were manually post-corrected for the ohmic losses by subtracting the IR_u product, where specifically mentioned.

Physical Characterization: XRD analysis was performed using a D8 Cobalt Bruker diffractometer with a Co-K_α source (1.78897 Å; 40 kV operating power, 25 mA operating current) with a scan rate 0.05° min^{-1} and a holder rotation rate of 15 rpm. Samples were thoroughly ground and evenly distributed over a low background sample holder.

Raman spectroscopic characterization was undertaken using a Renishaw Raman spectrometer with a green laser (514 nm) at 5% power and acquisition duration of 30 s. Samples for the analysis were ground and powders were evenly spread over a quartz slide support.

XPS measurements were completed using a Nexsa Surface Analysis System (Thermo Fisher Scientific) equipped with a monochromatic Al-K_α X-ray source (spot size 400 µm) at a power of 180 W ($15 \text{ kV} \times 12$ mA) and a pressure not exceeding 1×10^{-8} mbar. Survey spectra were recorded at a pass energy of 200 eV with a step size of 1 eV. High-resolution spectra were recorded at a pass energy of 50 eV with a step size of 0.1 eV. Powder samples were mounted by pressing them into recesses on a copper plate, ensuring that the powder surface was flat and leveled with the surface of the plate top; no electrical contact between the sample and instrument ground was provided. A low-energy dual-beam (ion and electron) flood source was used for charge neutralisation. Data processing was performed using Thermo Avantage software version 5.9913 (Thermo Fisher Scientific, East Grinstead, UK). The atomic concentrations of the detected elements were calculated by integrating corresponding peak areas and normalizing the latter using sensitivity factors stated by the manufacturer. The accuracy of quantitative analysis was 10%–15%. Binding energies were referenced to the aliphatic carbon C 1*s* peak at 248.8 eV; however, given the ambiguity in the position of the C–C component in the C 1*s* spectra for the samples examined herein, no significance should be attached to the absolute values of the reported binding energies.

SEM images and EDS data under SEM conditions were collected with an FEI Magellan–FEG instrument equipped with a Bruker Quantax silicon drift X-ray detector. Samples for the imaging were dispersed in 2-propanol and drop-cast onto a silicon slide, which was glued with a super glue and electrically connected by a copper tape to the aluminum SEM stud.

TEM data were acquired using a *Tecnai F20* microscope operating under 200 kV accelerating voltage of the electron-emission source. Analyzed samples were dispersed in ethanol and drop-cast onto a holey carbon-coated copper grids obtained from EM Resolutions.

XAS data were recorded on a multipole wiggler XAS beamline 12 ID at the Australian Synchrotron, ANSTO, in operational mode 1 using a Si (111) crystal for the Co and Fe K-edges. The beam energy was 3.0 GeV with a beam current of 200 mA. Samples for ex situ analysis were prepared as pressed powders by grinding and mixing with boron nitride. Data were collected in fluorescence mode for all edges. Energies were calibrated against the first inflection point of the iron foil at 7112 eV and cobalt foil at 7709 eV. In situ XAS analysis was undertaken using a cell reported by King et al.[60] and an Autolab PGSTAT101 (Metrohm) potentiostat at ambient temperature. Electrolyte solution flow was maintained by a Longer BT100-2J peristaltic pump. A "leak-free" Ag|AgCl|KCl (3.4 M) LF-1–100 reference electrode (Innovative Instruments) and high-surface-area nickel mesh were used as reference and auxiliary electrodes, respectively. Working and auxiliary electrode compartments were separated with a Zirfon membrane. During analysis, 1 M KOH electrolyte solution was pumped through the cell at a flow rate of approximately 5 mL^{-1}. A catalytic ink was prepared by adding 1 mg of the material to 1 mL of a 2-propanol:water (3:1 vol.) mixture containing 5 µL of PVDF–NMP and sonicated (Elmasonic, UC-7120L, 120 W) for 1 h. The ink was drop-cast onto the working electrode based on a SpectraCarb carbon fiber paper laminated into PET, with a circular area Ø 8 mm, defined by laser engraving, exposed to the electrolyte solution, as described elsewhere.[61] The catalyst loading was approximately 0.01 mg cm^{-2}. FT of the EXAFS data were calculated over a k range of 2–12. XAS data were analyzed using a combination of Sakura[62] for data conversion, Athena[63] and pySpline[64] for background subtraction.

ICP–MS analysis of the KOH electrolyte solution after stability testing of $Co_1Fe_1Se_n$ and ICP–OES analysis of $CoSe_n$ and $Co_1Fe_1Se_n$ materials was performed using *Perkin Elmer AvioNexION* 2000 and *PerkinElmer Avio 200* instruments, respectively. The later analysis used both axial and radial plasma views. Samples (5 mg) were digested in 5 mL aqua regia (HNO_3 70 wt%: HCl wt%, 36 = 1:4 vol) for 48 h prior to dilution to ≈5 wt% (OES), and 1 mL of the electrolyte was diluted 1:10 vol by 2 wt% HNO_3 (MS), and were analyzed for Co, Ni, Se (MS, OES), and Fe (OES). Raw analyte counts were standardized by means of a calibration curve constructed through systematic dilutions of commercially available stock solutions to concentrations in the range of 0.01–50 µg mL^{-1} in 5 wt% HNO_3 (OES) and 0.1–100 ng mL^{-1} in 2 wt% HNO_3 (MS). Analysis of blank solutions prepared using 2 or 5 wt% HNO_3 was used to measure the background and these counts were subtracted from all measurements. For ICP–MS, ^{45}Sc, ^{74}Ge, and ^{103}Rh ions were plumbed into the sample inlet as internal standards for ^{59}Co, ^{60}Ni, ^{56}Fe, and ^{82}Se isotopes, respectively, to allow correction for matrix effects and instrumental drift. For ICP–OES, results from the axial view were presented as it gave a higher signal-to-noise ratio while still showing a linear response at the concentrations analyzed. The measured difference between the axial and radial plasma views varied by not more than 3%.

Supporting Information

Supporting Information is available from the Wiley Online Library or from the author.

Acknowledgements

Some parts of this work were undertaken using the XAS and MEX beamlines of the Australian Synchrotron (ANSTO), Monash X-ray platform, and Monash Centre for Electron Microscopy. The financial support of the work by the Australian Research Council (grant no. FT200100317) and Australian Renewable Energy Agency (ARENA; Contract No. 2018/RND008) is acknowledged. The authors are grateful to Ms Brittany V. Kerr and Mr Jaydon Meilak from Swinburne University of Technology

for their help with collecting the XAS data, and to Mr. Kai Robinson from Monash University for his help with collecting the ICP–OES and ICP–MS data.

Open access publishing facilitated by Monash University, as part of the Wiley - Monash University agreement via the Council of Australian University Librarians.

Conflict of Interest

The authors declare no conflict of interest.

Data Availability Statement

The data that support the findings of this study are available from the corresponding author upon reasonable request.

Keywords

in situ, oxygen evolution reaction, selenide, X-ray absorption spectroscopy

Received: June 15, 2023
Revised: August 1, 2023
Published online: August 30, 2023

[1] J. D. Wiensch, J. John, J. M. Velazquez, D. A. Torelli, A. P. Pieterick, M. T. McDowell, K. Sun, X. Zhao, B. S. Brunschwig, N. S. Lewis, *ACS Energy Lett.* **2017**, *2*, 2234.
[2] T. Zhang, M.-Y. Wu, D.-Y. Yan, J. Mao, H. Liu, W.-B. Hu, X.-W. Du, T. Ling, S.-Z. Qiao, *Nano Energy* **2018**, *43*, 103.
[3] Y. Sun, T. Zhang, X. Li, Y. Bai, X. Lyu, G. Liu, W. Cai, Y. Li, *Adv. Mater. Interfaces* **2018**, *5*, 1800473.
[4] W. Sheng, H. A. Gasteiger, Y. Shao-Horn, *J. Electrochem. Soc.* **2010**, *157*, B1529.
[5] N. Mahmood, Y. Yao, J.-W. Zhang, L. Pan, X. Zhang, J.-J. Zou, *Adv. Sci.* **2018**, *5*, 1700464.
[6] X. Y. Zhang, J. Y. Xie, Y. Ma, B. Dong, C. G. Liu, Y. M. Chai, *Chem. Eng. J.* **2022**, *430*, 132312.
[7] X. Li, F. C. Walsh, D. Pletcher, *Phys. Chem. Chem. Phys.* **2011**, *13*, 1162.
[8] F. Song, L. Bai, A. Moysiadou, S. Lee, C. Hu, L. Liardet, X. Hu, *J. Am. Chem. Soc.* **2018**, *140*, 7748.
[9] J. Mohammed-ibrahim, H. Moussab, *J. Energy Chem.* **2021**, *56*, 299.
[10] Z. Chen, X. Duan, W. Wei, S. Wang, B. J. Ni, *J. Mater. Chem. A* **2019**, *7*, 14971.
[11] L. Wu, J. P. Hofmann, *ACS Energy Lett.* **2021**, *6*, 2619.
[12] Q. Kang, M. Li, J. Shi, Q. Lu, F. Gao, *ACS Appl. Mater. Interfaces* **2020**, *10*, 18.
[13] S. Anantharaj, S. Noda, *Int. J. Hydrogen Energy* **2020**, *45*, 15763.
[14] J. Bi, H. Ying, J. Hao, Z. Li, *Curr. Opin. Electrochem.* **2022**, *33*, 100963.
[15] L. Chen, Y. Wang, X. Zhao, Y. Wang, Q. Li, Q. Wang, Y. Tang, Y. Lei, *J. Mater. Sci. Technol.* **2022**, *110*, 128.
[16] B. Singh, A. Yadav, A. Indra, *J. Mater. Chem. A* **2022**, *10*, 3843.
[17] A. Karmakar, H. S. Chavan, S. M. Jeong, J. S. Cho, *Adv. Energy Sustainability Res.* **2022**, *3*, 2200071.
[18] J. Huang, S. Wang, J. Nie, C. Huang, X. Zhang, B. Wang, J. Tang, C. Du, Z. Liu, J. Chen, *Chem. Eng. J.* **2021**, *417*, 128055.
[19] S. Poorahong, D. J. Harding, S. Keawmorakot, M. Siaj, *J. Electroanal. Chem.* **2021**, *897*, 115568.
[20] S. Liu, Y. Jiang, M. Yang, M. Zhang, Q. Guo, W. Shen, R. He, M. Li, *Nanoscale* **2019**, *11*, 7959.
[21] Y. Zhao, B. Jin, Y. Zheng, H. Jin, Y. Jiao, S. Z. Qiao, *Adv. Energy Mater.* **2018**, *8*, 1801926.
[22] X. Cao, J. E. Medvedeva, M. Nath, *ACS Appl. Energy Mater.* **2020**, *3*, 3092.
[23] W. Zong, R. Lian, G. He, H. Guo, Y. Ouyang, J. Wang, F. Lai, Y. E. Miao, D. Rao, D. Brett, T. Liu, *Electrochim. Acta* **2020**, *333*, 135515.
[24] A. El Jaouhari, A. Slassi, B. Zhang, A. Pershin, W. Liu, D. Cornil, X. Liu, J. Zhu, *J. Power Sources* **2021**, *514*, 230596.
[25] M.-Q. Yang, J. Wang, H. Wu, G. W. Ho, *Small* **2018**, *14*, 1703323.
[26] X. Xia, L. Wang, N. Sui, V. L. Colvin, W. W. Yu, *Nanoscale* **2020**, *12*, 12249.
[27] S. Wan, W. Jin, X. Guo, J. Mao, L. Zheng, J. Zhao, J. Zhang, H. Liu, C. Tang, *ACS Sustainable Chem. Eng.* **2018**, *6*, 15374.
[28] M. Chatti, A. M. Glushenkov, T. Gengenbach, G. P. Knowles, T. C. Mendes, A. V. Ellis, L. Spiccia, R. K. Hocking, A. N. Simonov, *Sustainable Energy Fuels* **2018**, *2*, 1561.
[29] N. Du, Q. Yang, Q. Liang, *Inorg. Chem. Commun.* **2022**, *144*, 109918.
[30] C. Yan, H. Shan, H. Yang, W. Zhang, S. B. Wang, Y. Zhang, J. Qin, W. Li, W. Xiao, Z. Zhou, X. Li, *ChemElectroChem* **2021**, *8*, 4745.
[31] Y. Zhang, C. Zhang, Y. Guo, D. Liu, Y. Yu, B. Zhang, *J. Mater. Chem. A* **2019**, *7*, 2536.
[32] K. Zhang, Y. Li, S. Deng, S. Shen, Y. Zhang, G. Pan, Q. Xiong, Q. Liu, X. Xia, X. Wang, J. Tu, *ChemElectroChem* **2019**, *6*, 3530.
[33] Y. Wang, S. Li, D. Zhang, F. Tan, L. Li, G. Hu, *J. Alloys Compd.* **2022**, *889*, 161696.
[34] W. Li, X. Gao, D. Xiong, F. Wei, W.-G. Song, J. Xu, L. Liu, *Adv. Energy Mater.* **2017**, *7*, 1602579.
[35] S. Prabhakaran, J. Balamurugan, N. H. Kim, J. H. Lee, *Small* **2020**, *16*, 2000797.
[36] Y. Liu, H. Cheng, M. Lyu, S. Fan, Q. Liu, W. Zhang, Y. Zhi, C. Wang, C. Xiao, S. Wei, B. Ye, Y. Xie, *J. Am. Chem. Soc.* **2014**, *136*, 15670.
[37] J. Suntivich, K. J. May, H. A. Gasteiger, J. B. Goodenough, Y. Shao-Horn, *Science* **2011**, *334*, 1383.
[38] M. Chatti, T. Gengenbach, R. King, L. Spiccia, A. N. Simonov, *Chem. Mater.* **2017**, *29*, 3092.
[39] E. Charnetskaya, M. Chatti, B. Kerr, T. Tran-Phu, T. Nguyen, P. Cherepanov, D. Hoogeveen, B. Johannessen, A. Tricoli, D. Macfarlane, R. Hocking, A. Simonov, *ACS Sustainable Chem. Eng.* **2022**, *10*, 7117.
[40] C. W. Kung, C. Y. Lin, T. J. Li, R. Vittal, K. C. Ho, *Procedia Eng.* **2011**, *25*, 847.
[41] T. Tran-Phu, H. Chen, R. Daiyan, M. Chatti, B. Liu, R. Amal, Y. Liu, D. R. Macfarlane, A. N. Simonov, A. Tricoli, *ACS Appl. Mater. Interfaces* **2022**, *14*, 33130.
[42] H. Li, X. Qian, C. Zhu, X. Jiang, L. Shao, L. Hou, *J. Mater. Chem. A* **2017**, *5*, 4513.
[43] C. E. Campos, J. de Lima, T. Grandi, K. Machado, P. Pizani, *Physica B* **2002**, *324*, 409.
[44] Z. Qin, C. Zhang, S. O'Malley, K. Lo, T. Zhou, S. W. Cheong, *Solid State Commun.* **2010**, *150*, 768.
[45] J. Yang, H. Gao, S. Men, Z. Shi, Z. Lin, X. Kang, S. Chen, *Adv. Sci.* **2018**, *5*, 1800763.
[46] Y. Tang, X. Li, H. Lv, D. Xie, W. Wang, C. Zhi, H. Li, *Adv. Energy Mater.* **2020**, *10*, 2000892.
[47] Z. Li, X. Hu, Z. Shi, Z. Wang, J. Lu, *Energy Technol.* **2021**, *9*, 2100462.
[48] J. Jiang, L. Li, *Mater. Lett.* **2007**, *61*, 4894.
[49] M. Teo, P. C. Wong, L. Zhu, D. Susac, S. A. Campbell, K. A. R. Mitchell, R. R. Parsons, D. Bizzotto, *Appl. Surf. Sci.* **2006**, *253*, 1130.

[50] M. C. Biesinger, B. P. Payne, A. P. Grosvenor, L. W. M. Lau, A. R. Gerson, R. S. C. Smart, *Appl. Surf. Sci.* **2011**, *257*, 2717.
[51] H. Shan, J. Qin, Y. Ding, H. M. K. Sari, X. Song, W. Liu, Y. Hao, J. Wang, C. Xie, J. Zhang, X. Li, *Adv. Mater.* **2021**, *33*, 2102471.
[52] L. A. Saucedo, J. K. Clark, J. S. R. V. Winfred, G. F. Strouse, M. Shatruk, *J. Phys. Chem. C* **2021**, *125*, 25784.
[53] F. Dionigi, J. Zhu, Z. Zeng, T. Merzdorf, H. Sarodnik, M. Gliech, L. Pan, W. Li, J. Greeley, P. Strasser, *Angew. Chem. Int. Ed.* **2021**, *60*, 14446.
[54] F. Dionigi, Z. Zeng, I. Sinev, T. Merzdorf, S. Deshpande, M. B. Lopez, S. Kunze, I. Zegkinoglou, H. Sarodnik, D. Fan, A. Bergmann, J. Drnec, J. F. de Araujo, M. Gliech, D. Teschner, J. Zhu, W. X. Li, J. Greeley, B. Roldan Cuenya, P. Strasser, *Nat. Commun.* **2020**, *11*, 2522.
[55] K. N. Dinh, M. Chatti, T. D. Nguyen, D. A. Hoogeveen, D. R. Macfarlane, A. N. Simonov, *ACS Energy Lett.* **2022**, *7*, 3910.
[56] S. Anantharaj, S. R. Ede, K. Sakthikumar, K. Karthick, S. Mishra, S. Kundu, *ACS Catal.* **2016**, *6*, 8069.
[57] M.-R. Gao, W.-T. Yao, H.-B. Yao, S.-H. Yu, *J. Am. Chem. Soc.* **2009**, *131*, 7486.
[58] S. Johnston, L. Kemp, B. Turay, A. N. Simonov, B. H. R. Suryanto, D. R. MacFarlane, *ChemSusChem* **2021**, *14*, 4793.
[59] D. Simondson, M. Chatti, S. A. Bonke, M. F. Tesch, R. Golnak, J. Xiao, D. A. Hoogeveen, P. V. Cherepanov, J. L. Gardiner, A. Tricoli, D. R. MacFarlane, A. N. Simonov, *Angew. Chem. Int. Ed.* **2021**, *60*, 15821.
[60] H. J. King, M. Fournier, S. A. Bonke, E. Seeman, M. Chatti, A. N. Jumabekov, B. Johannessen, P. Kappen, A. N. Simonov, R. K. Hocking, *J. Phys. Chem. C* **2019**, *123*, 28533.
[61] D. Simondson, M. Chatti, J. L. Gardiner, B. V. Kerr, D. A. Hoogeveen, P. V. Cherepanov, I. C. Kuschnerus, T. D. Nguyen, B. Johannessen, S. L. Y. Chang, D. R. Macfarlane, R. K. Hocking, A. N. Simonov, *ACS Catal.* **2022**, *12*, 12912.
[62] P. Kappen, R. Gary, *Sacura: Data Explorer For X-ray Absorption Spectroscopy (XAS)*, Australian Synchrotron, Melbourne **2013**.
[63] B. Ravel, M. Newville, *J. Synchrotron Radiat.* **2005**, *12*, 537.
[64] A. Tenderholt, B. Hedman, K. O. Hodgson, *AIP Conf. Proc.* **2007**, *882*, 105.
[65] H. Li, D. Gao, X. Cheng, *Electrochim. Acta* **2014**, *138*, 232.
[66] Y. Tang, Z. Zhao, X. Hao, Y. Wang, Y. Liu, Y. Hou, Q. Yang, X. Wang, J. Qiu, *J. Mater. Chem. A* **2017**, *5*, 13591.
[67] M. Basu, Z. W. Zhang, C. J. Chen, P. T. Chen, K. C. Yang, C. G. Ma, C. C. Lin, S. F. Hu, R. S. Liu, *Angew. Chem., Int. Ed.* **2015**, *54*, 6211.
[68] H. Zhang, Y. Cheng, Q. Zhang, W. Ye, X. Yu, M. S. Wang, *ACS Nano* **2021**, *15*, 10107.